Three-dimensional theory on light-induced near-field dynamics in a metal film with a periodic array of nanoholes

Roland Müller, Viktor Malyarchuk, and Christoph Lienau
Max-Born-Institut für Nichtlineare Optik und Kurzzeitspektroskopie, Max-Born-Strasse 2A, 12489 Berlin, Germany
(Received 9 May 2003; revised manuscript received 29 August 2003; published 18 November 2003)

We present a theoretical study of ultrafast light propagation through a periodic array of nanoapertures in an optically thick metal film. Studying the propagation of 10-fs pulses shorter than the damping time of surface plasmon excitations at the interfaces of the metal film, we find pronounced temporal oscillations in the transmitted light. The oscillations reflect the coupling of surface plasmon polaritons at both interfaces via photon tunneling through the nanohole channel. The diameter of the nanoholes is the main parameter governing the period and damping of these oscillations. Radiation damping of surface plasmon excitations through scattering at the nanoholes is identified as an important damping mechanism. Our results give insight into the physics of light transmission through nanohole gratings and clear guidelines for designing the optical properties of these nanostructures.

DOI: 10.1103/PhysRevB.68.205415 PACS number(s): 73.20.Mf, 78.66.Bz, 81.07.−b, 02.70.Bf

I. INTRODUCTION

The interaction between light and metal films exhibiting periodic spatial modulation on the subwavelength scale has attracted much attention in recent years. These studies give evidence for extraordinarily high light transmission[1,2] and suggest the existence of photonic energy band gaps (i.e., prohibited propagation states for light within a specific frequency range) (Refs. 1–6) in nanostructured metallic films. Both effects have been connected with surface plasmon polaritons (SPP's), i.e., electromagnetic surface waves that propagate along the interface between a metal and a dielectric.[7–9] These waves are due to charge oscillations at the surface of the metal driven by the incident light. The electromagnetic field and the associated charge oscillations (surface plasmons) set up a coupled surface state, the SPP, characterized by a specific energy-momentum dispersion relation.

In thin periodically corrugated metal films both band gap formation and enhanced light transmission are linked to the coupling between SPP waves at the top and bottom interfaces of the film. Therefore, such gratings open up a possibility to study coupling effects between SPP waves on their top and bottom surfaces.[10,11] Whereas in optically thick metal films, with a thickness much larger than the skin depth, SPP waves at both interfaces do not interfere, SPP waves in thin films can generally not be considered as independent entities, but constitute a pair of coupled oscillators with an energy splitting given by the coupling strength. The underlying physics is similar to that of other coupled two-mode systems, e.g., two coupled mechanical pendulums or electron and hole states in semiconductor double-quantum-well nanostructures.

Such coupling effects also occur in *thick* metal films with periodic nanoaperture arrays, e.g., in one-dimensional slit arrays (lamellar transmission gratings) or in periodic two-dimensional hole arrays (crossed gratings or ''bigratings'').[1,12,13] Here the interaction between SPP modes at both interfaces occurs via the coupling of light through the nanoapertures. This interaction between SPP waves is assumed to be the reason for the extraordinarily high transmission found by Ebbesen *et al.* in periodic subwavelength hole arrays.[1] The measured far-field transmission was much larger than that expected from diffraction theory for an isolated hole.[1,14,15]

As SPPs are surface waves, most of their energy is bound in the electromagnetic near field, close to the metal/dielectric interface. This suggests that near-field scanning optical microscopy (NSOM) is a particularly suitable tool for studying SPP properties. In Ref. 16 light transmission through a gold film with periodic hole arrays was measured close to the metal surface employing a metal-coated fiber tip. In particular, interference patterns of counterpropagating SPP waves were observed along the polarization direction of the incident light field. Excitation of SPP waves was also studied in experiments probing transmission through single holes.[17]

The theoretical description of enhanced light transmission has attracted considerable attention over the last years. Time-independent simulations of light transmission in metallic films with one-dimensional slits[18–20] or periodic hole arrays[13,21–24] have been reported using different numerical techniques. In addition to SPP waves at the top and bottom interfaces also modes inside the slits or cylindrical nanohole channels can be excited.[25] In one-dimensional gratings, propagating transverse electromagnetic (TEM) modes exist, while in nanohole arrays with sufficiently small hole diameter, only exponentially damped light fields are present inside the holes.[21] For bigratings, a *detailed* theoretical understanding of coupling effects between SPP waves on opposite surfaces is still lacking. In particular, the time-dependent coupling of SPP's through nanoholes is still under much debate.[15] A physical description of this process requires a time-dependent description of the energy transmission through the nanoapertures and its connection with energy transport on the surfaces. To resolve these dynamic coupling effects we follow in this work an approach that is well known from time-resolved quantum-beat spectroscopy. The coupled system is impulsively excited by an ultrashort light pulse, shorter in duration than the relevant damping and coupling times, and the subsequent light scattering dynamics

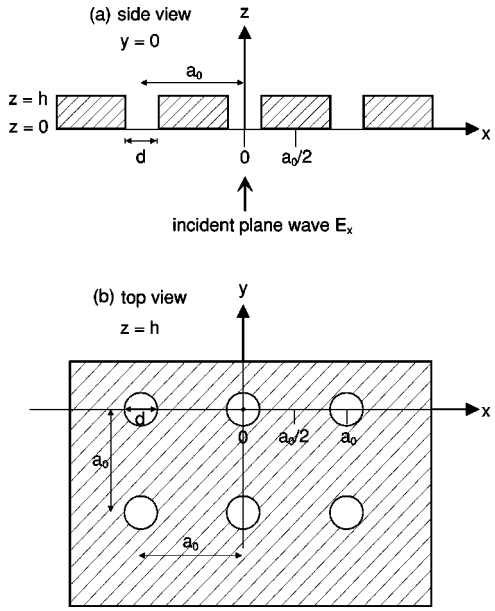

FIG. 1. Schematic of a freestanding metal film, perforated with an array of holes. a_0 is the lattice constant, d the hole diameter, and h the thickness of the film. (a) Cross section through the metal film (x-z plane). The input wave is polarized along x and illuminates the bottom metal surface at normal incidence. (b) Top view of the metal film (x-y plane).

is investigated in fully three-dimensional finite-difference time-domain simulations.

The aim of this paper is to study the intrinsic SPP coupling mechanisms in a metallic film perforated with nanometer-sized holes that is impulsively excited with a femtosecond light pulse. Here, the carrier wavelength of the pulse is larger than the cutoff wavelength of the cylindrical hole channel. The dynamic linear response of the material polarization to the impulsive excitation is calculated inside the nanoholes as well as in the immediate vicinity of the metallic film, i.e., in the near-field region. A detailed description of the time-dependent interaction between plasmon-induced surface waves and modes inside the holes is given. Coupling between SPP excitation at both interfaces of the metal film is evidenced via pronounced temporal oscillations in the field intensity transmitted through the nanoholes. We find that the diameter of the nanoholes plays a key role for both the dynamics of the plasmon coupling as well as for the scattering of SPP excitations into far-field radiation. The spatial dependence of the electromagnetic near-field profiles is simulated, showing pronounced spatial interference of SPP waves, in good agreement with recent experiments.[16]

II. THEORETICAL MODEL

In the following, we study light propagation through a *freestanding* silver film of thickness $h=100$ nm, perforated with a periodic hole array of period $a_0=500$ nm and hole diameters d between 100 and 300 nm. The film is assumed to extend to infinity in the x and y directions. An x-polarized coherent plane wave, propagating in the z direction, illuminates the metal film at normal incidence: see Fig. 1. The time-dependent intensity of the incident electric field is a Gaussian pulse of 10 fs full width at half maximum (FWHM).

Light propagation in the metal is described by Maxwell's equations, which are coupled to an equation for the light-induced oscillations of quasifree electrons in the metal (Drude model):

$$\vec{\nabla}\times\vec{E}=-\mu_0\frac{\partial\vec{H}}{\partial t}, \tag{1a}$$

$$\vec{\nabla}\times\vec{H}=\varepsilon_0\frac{\partial\vec{E}}{\partial t}+\vec{J}, \tag{1b}$$

$$\frac{\partial\vec{J}}{\partial t}+\gamma\vec{J}=\varepsilon_0\omega_p^2\vec{E}, \tag{1c}$$

where $\vec{E}$ and $\vec{H}$ are the electric and magnetic field vectors, respectively, and $\vec{\nabla}$ is the Nabla differential operator. $\vec{J}$ is a current density (A/cm^2) corresponding to the time derivative $\vec{J}=\partial\vec{P}/\partial t$ of the metal polarization. ω_p is the plasma frequency of the metal and γ denotes a damping rate characterizing the Ohmic absorption losses that heat the metal. ε_0 and μ_0 are the free-space permittivity and magnetic permeability. In free space, around the metal film and in its air-filled holes, light propagation is described by Eqs. (1a) and (1b) with $\vec{J}\equiv 0$.

We take the following approximate expression for the complex dielectric constant of the metal (see, e.g., Ref. 26):

$$\varepsilon_1(\omega)=1-\frac{\omega_p^2}{\omega^2+i\gamma\omega}, \tag{2}$$

where $\hbar\omega_p=8.6$ eV (i.e., $\lambda_p=144$ nm), $\hbar\gamma=0.075$ eV in the present case of silver and ω is the (circular) frequency of light. In the energy range considered, the Drude model is reasonably close to the experimental values for the dielectric function of silver.[27] The use of such a semiclassical continuum model [Eq. (1c)] is justified, as the dimensions of the nanostructures considered (~ 100 nm) are much larger than the electron mean free path inside the metal.

The time-dependent electric field and Poynting vector inside the metal as well as below and above it are numerically calculated applying a three-dimensional (3D) finite-difference time-domain code (FDTD) to Eqs. (1a)–(1c); see, e.g., Ref. 28. The respective space grid is composed of 200 (x direction)$\times$200 (y)$\times$210 (z) cells with space increments $\Delta x=\Delta y=\Delta z=2.5$ nm and a time increment of $\Delta t=4\times10^{-3}$ fs, corresponding to a computational working volume of 0.50 μm$\times$0.50 μm$\times$0.525 μm of an array period (unit cell) around a single hole. Periodic boundary conditions are applied to the sides of the unit cell being parallel to the x and y axes, whereas perfectly matched layer (PML) conditions[29] are applied to the top and bottom boundaries of the unit cell, i.e., free-space propagation of the light field above and below the metallic film. The numerical values of the parameters (h, a_0, d, and wavelength λ) used in this paper are chosen similar to the experimental values, taking

the limited resources of our workstation into account. The stability of the calculations is limited to about 100 fs for quasi-cw excitation and to more than 200 fs for short-pulse excitation.

Here we focus on calculations in the wavelength interval between 510 and 560 nm, around the (1, 0) metal/air plasmon resonance at $\lambda_{res} \approx 522$ nm, given by

$$\lambda_{res} \cong \frac{a_0}{\sqrt{1+1/\varepsilon_1'}}, \tag{3}$$

which follows from the SPP dispersion for a planar metal/air interface.[8] $\varepsilon_1' \approx 1-(\lambda_{res}/\lambda_p)^2$ denotes the real part of $\varepsilon_1 = \varepsilon_1' + i\varepsilon_1''$. Equation (3) includes no details about the spatial profile of the metal film such as width and depth of the holes. Thus λ_{res} is only an approximate value, which we find, however, to be fairly accurate. Since $\lambda_{res} > a_0$ holds for the (1,0) SPP resonance, only the T_{00} far-field diffraction mode of the bigrating is excited in this wavelength interval.[30]

Another parameter of interest is the propagation length $L_{sp} = 1/2|k_{sp,x}''|$ at which the intensity of a propagating SPP wave on a *planar* metal/air interface decreases to $1/e$, due to energy absorption in the metal.[8] From

$$L_{sp}^{-1} \cong \left| \frac{\omega \varepsilon_1''}{c\varepsilon_1'^2} \left(\frac{\varepsilon_1'}{\varepsilon_1'+1} \right)^{3/2} \right|,$$

one obtains $L_{sp} \approx 27\ \mu$m for silver at $\lambda_{res} = 522$ nm (Ref. 8). This estimate of L_{sp} falls within the range of experimental values of 20–50 μm for the SPP propagation length measured on a planar silver surface in the wavelength interval from 500 to 600 nm (Ref. 31). $k_{sp,x} = k_{sp,x}' + ik_{sp,x}''$ denotes the component of the complex SPP wave vector along the x axis. From $L_{sp} = 27\ \mu$m the damping time $T_{sp} = L_{sp}/v_{ph} \approx 93$ fs is deduced using the phase velocity $v_{ph} = \omega/k_{sp,x}' \approx 0.96c$, where $k_{sp,x}' = 2\pi/a_0$. Below, T_{sp} will be compared to SPP damping constants for propagation on surfaces perforated with holes.

In the following we will present theoretical results for (i) a continuous-wave input field and (ii) for a femtosecond input pulse. In both cases an incident optical plane wave polarized along the x axis is assumed. Its electric and magnetic field strengths are given by the real functions $E_{x,in}(z,t) = A_{in}\cos[\omega t - (2\pi/\lambda)z]$ and $H_{y,in}(z,t) = \sqrt{\varepsilon_0/\mu_0}E_{x,in}(z,t)$. Here, $\omega = 2\pi c/\lambda$ and A_{in} is a Gaussian-shaped function $A_{in} = A_0 \exp[-2\ln 2\{(t-t_0-z/c)/\tau_0\}^2]$, where A_0 is the field amplitude. The parameters $t_0 = 30$ fs and $\tau_0 = 10$ fs denote an arbitrarily chosen delay time and the pulse width, respectively. Continuous-wave (steplike) excitation corresponds to $A_{in} = A_0 \exp[-2\ln 2\{(t-t_0-z/c)/\tau_0\}^2]$, if $t < t_0 - z/c$, and $A_{in} = A_0 = \text{const}$, if $t \geqslant t_0 - z/c$. The results for cw illumination are used to numerically estimate the SPP resonance. At this resonance, fs-pulse excitation will then be studied.

The temporal and spatial evolution of the field energy inside a nanohole channel in a metal of finite conductivity is accompanied by a Poynting flow $S_z = (\vec{E} \times \vec{H})_z$ (W/cm^2), directed along the z axis; see Sec. III E. On the other hand, the Poynting vector component $S_x = (\vec{E} \times \vec{H})_x$ in the lower and upper surfaces of the metal film characterizes the energy transport along the x direction. S_x is an odd function of x that changes sign at the center of a hole. Thus, S_x, on both the right and left sides of each hole; is directed either away from or towards this hole; i.e., the hole acts as a source or a sink, respectively. The third component S_y is in most cases negligible.

$s_z = (1/F)\int S_z(x,y)dxdy$ is the *mean* value of S_z inside one hole, where the integral is taken over the hole cross section of area F. The time average of s_z, taken over one cycle $T = 2\pi/\omega$, is indicated by a bar, $\overline{s_z}$. Finally, a normalized quantity $\overline{s_{z,norm}} = \overline{s_z}/\overline{s_{in,\max}}$ is introduced, where $\overline{s_{in,\max}} = c\varepsilon_0 A_0^2/2$ denotes the power density at the peak of the input signal. In addition to $\vec{S}$, the energy density W_e (Ws/cm^3) of the electric field is of interest. For instance, $W_{ex} = \frac{1}{2}\varepsilon_0 E_x^2$ describes the instantaneous energy density of E_x. As above, we define a mean value w_{ex}, a time average $\overline{w_{ex}}$, and a density $\overline{w_{ex,norm}}$, normalized to $\overline{w_{in,\max}} = \varepsilon_0 A_0^2/4$.

In the following the spatio-temporal evolution of the electric field and the Poynting vector will be considered, when the nanostructured metal film is excited with a 10-fs pulse. The results given below correspond to different hole diameters (100–300 nm).

III. RESULTS

A. SPP resonance

Most interesting light field dynamics can be expected at or close to a plasmon resonance where the coupling between the fields on the upper and lower surfaces should be strongest. We first identify this resonance wavelength by studying the wavelength-dependent energy flux transmitted through a nanohole with 100 nm diameter connecting both surfaces.

Figure 2 shows the time evolution of the energy flow density $\overline{s_{z,norm}}$ inside a hole at the bottom surface, $z = 0$ (dashed curves), and at the top surface, $z = h$ (solid curves), for various wavelengths under *continuous-wave* excitation. $\overline{s_{z,norm}}$ corresponds to a real power flow, damped along the guide axis. The final value of $\overline{s_{z,norm}}$ is maximal at $\lambda = 530$ nm [see Fig. 2(d)], which is close to the approximate value of $\lambda_{res} \approx 522$ nm for the (1, 0) plasmon resonance deduced from Eq. (3). Figure 2(d) also indicates that $\overline{s_{z,norm}} \approx 1.5$ in the upper hole after the energy flow has reached a constant level. This means that 1.5 times more light intensity is transmitted through the air-filled channel in the metallic film than is directly incident on the aperture of the hole at the bottom interface.

A different behavior of $\overline{s_{z,norm}}$ is seen in Figs. 2(a) and 2(f), corresponding to the end points of the considered wavelength interval, i.e., $\lambda = 510$ and 560 nm. They show only small values of $\overline{s_{z,norm}}$; i.e., the resonance condition for SPP excitation is no longer fulfilled.

B. SPP coupling

We now proceed with calculating the time evolution of light propagation under *impulsive* excitation conditions: a

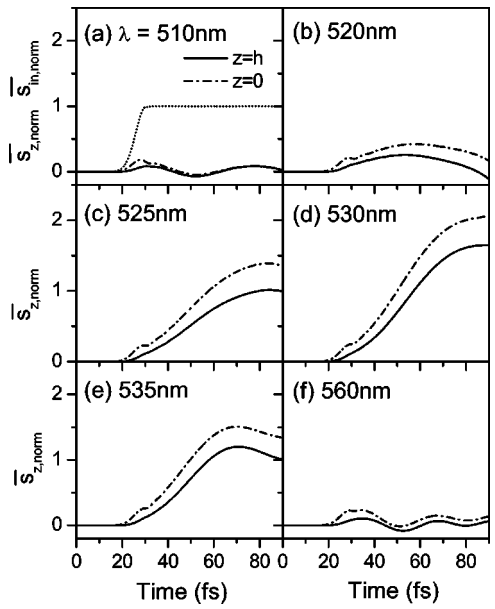

FIG. 2. Normalized mean *photon flux* density $\overline{s_{z,norm}}$ directed along z, vs time inside a hole at the bottom ($z=0$, dashed curves) and on the top ($z=h$, solid curves) of the metal film for various wavelengths of the incident field, between $\lambda=510$ and 560 nm, (a)–(f). The input power density is a steplike function (dotted curve) shown in (a).

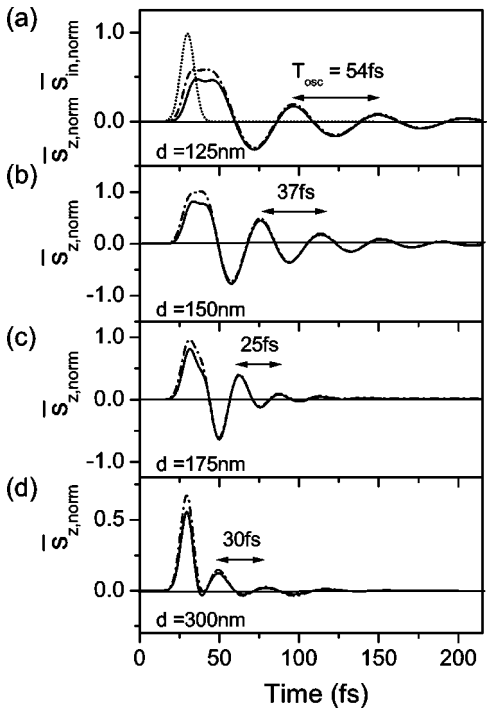

FIG. 3. Normalized mean *photon flux* density directed along z, $\overline{s_{z,norm}}$, vs time in a hole at the bottom ($z=0$, dashed curves) and on the top ($z=h$, solid curves) of the metal film for various hole diameters of $d=125$–300 nm, (a)–(d). The incident signal (dotted curve) is a 10-fs pulse with peak intensity at $t=30$ fs, shown in (a).

10-fs pulse with a carrier wavelength of $\lambda=530$ nm is normally incident on the lower metal surface. The pulse duration is chosen to be shorter than the expected SPP damping time of a few tens femtoseconds. Under such conditions, a SPP excitation at the bottom interface is impulsively driven by the incident field, and the propagation dynamics of this excitation are then simulated numerically.

Figure 3 shows the normalized mean photon flux density $\overline{s_{z,norm}}$ in the holes on the lower (dashed curves) and upper (solid curves) surfaces for various hole diameters d, namely, (a) $d=125$ nm, (b) $d=150$ nm, (c) $d=175$ nm, and (d) $d=300$ nm. Figure 3(a) also includes the power density of the input pulse, $\overline{s_{in,norm}}$, normalized to $\overline{s_{in,\max}}$. Figures 3(a)–3(d) indicate damped periodic oscillations of $\overline{s_{z,norm}}$ following the impulsive excitation. As can be seen from Figs. 3(a)–3(c), the oscillation period $T_{\rm osc}$ of $\overline{s_{z,norm}}$ decreases with increasing hole diameter and the time decrease of the oscillation peaks becomes stronger with increasing hole diameter. Outside of the holes, $\overline{S_z}$ is much smaller than inside the holes. At all times, $\overline{S_z}$ points towards the metal, reflecting energy absorption due to Ohmic losses by the metal.

The total loss causing the damping of the oscillations includes two essential contributions: (i) the absorption (Ohmic) loss associated with the damping factor γ of the metal and (ii) the scattering loss depending on d. We assume an exponential decrease due to absorption and scattering losses and introduce the three decay times $T_{\rm tot}$, $T_{\rm abs}$, and $T_{\rm scat}$, corresponding to the total loss, absorption loss, and scattering loss, respectively. Then the total decay time is given as

$$1/T_{\rm tot}=1/T_{\rm abs}+1/T_{\rm scat}. \tag{4}$$

If the total hole area is small compared to that of the metal surfaces, $T_{\rm abs}$ is approximately given by the decay time of a SPP wave propagating on a *planar* metal surface, T_{sp}. For $\lambda=530$ nm one obtains a damping time $T_{sp}=93$ fs. Plotting the values of $|\overline{s_{z,norm}}|$ from Fig. 3 on a logarithmic scale, one finds a nearly exponential decay of the peak values of $\overline{s_{z,norm}}$ with time. Thus, the envelope curves of $\overline{s_{z,norm}}$ are approximately given as $\exp(-t/T_{\rm tot})$. The values of $T_{\rm tot}$ then are extracted from these logarithmic plots for the different hole diameters. The scattering time $T_{\rm scat}$ is taken from Eq. (4) with $T_{\rm abs}=93$ fs.

C. Radiative SPP damping and SPP coupling strength

In Fig. 4(a), the total decay time of the damped oscillations, $T_{\rm tot}$, is shown together with $T_{\rm scat}$ on a double-logarithmic scale. For small hole diameters, $d=125$ nm, $T_{\rm tot}$ is much smaller than $T_{\rm scat}$, indicating that in this case the absorption in the metal is the major loss process. On the other hand, scattering is the dominant loss mechanism for large hole diameters, as can be seen for $d=300$ nm, where $T_{\rm scat}\approx T_{\rm tot}$. Figure 4(a) also shows that, in the interval from $d=125$ to 175 nm, the $T_{\rm scat}$ curve is close to the solid line proportional to the inverse of the fourth power of the hole diameter, d^{-4}. This agrees well with the experimentally observed dependence for the scattering cross section σ of single nanometer-sized holes in metal films illuminated by SPP waves with a wavelength of $\lambda=780$ nm (Ref. 6). In Fig. 4(b), we deduce from these data a relative scattering time

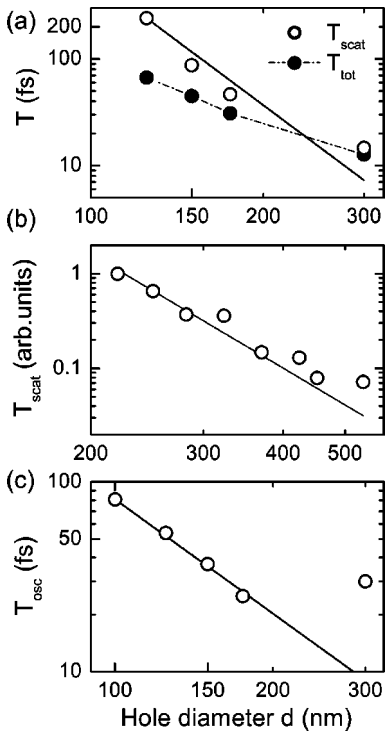

FIG. 4. (a) Log-log plot of the decay times vs hole diameter taken from the damped periodic oscillations of Fig. 3. Solid circles: total damping time T_{tot} indicating absorption and scattering losses. Open circles: scattering time of surface waves T_{scat} estimated from T_{tot} with $T_{\mathrm{abs}}=93$ fs. Solid line: $T\propto d^{-4}$. (b) Open circles: normalized scattering times of surface plasmon waves at single nanoholes vs hole diameter, deduced from *experimental* data given in Ref. 6. Solid line: $T\propto d^{-4}$. (c) Open circles: oscillation period T_{osc} vs hole diameter taken from the periodic oscillations of Fig. 3. Solid line: $T\propto d^{-2}$.

$T_{\mathrm{scat}}(d)=\sigma(220\ \mathrm{nm})/\sigma(d)$, normalized to the cross section for $d=220$ nm. For small diameters, T_{scat} decreases with d^{-4}, which indicates a Rayleigh-like scattering of the quasi-2D surface-bound SPP waves.[32] For larger hole diameters $d\geqslant 400$ nm, i.e., $d/\lambda\geqslant 0.5$, one finds a weaker dependence on d, indicating that the Rayleigh limit is no longer applicable. This deviation from the d^{-4} dependence can also be seen in our theoretical simulation for $d=300$ nm [Fig. 4(a)]. As in the experiment,[6] strong deviations from the Rayleigh limit are found for $d/\lambda\geqslant 0.5$.

In addition, we have calculated the time dependence of $\overline{s_{z,norm}}$ for vanishing absorption losses, setting $\gamma=0$ in Eq. (3c). We find the same oscillation periods as in Fig. 3, but now the damping is weaker due to the absence of absorption losses. For large d, the calculated damping times agree well with the values of T_{scat} in Fig. 4(a). For $d\leqslant 150$ nm, some deviations are observed due to the limited numerical stability of the FDTD calculations.

Figure 4(c) shows the dependence of the oscillation period T_{osc} on the hole diameter d. For $d\leqslant 175$ nm, T_{osc} decreases with d^{-2}. This means that the oscillation period scales with the inverse cross section of the hole provided the hole diameter is sufficiently small. Deviations from the d^{-2} dependence are observed for the largest hole diameter $d=300$ nm.

These damped oscillations are a clear manifestation of the coupling between SPP waves on the top and bottom interfaces of the metal nanostructure, mediated by the nanoapertures. Figures 3(a)–3(c) show the periodic change of the energy flux between upward and downward directions. Through the nanohole channel optical energy is transferred between bottom and top side generating SPP fields at the interfaces until the total field energy has decayed due to Ohmic and scattering losses. This picture reminds one of a pair of weakly coupled pendula with a beat frequency that is inversely proportional to the coupling parameter. The increase of the coupling proportional to d^2 simply reflects the increase in field energy inside the nanohole channel with the channel cross section. For larger hole diameters ($d\geqslant 200$ nm) the losses at the exit of the nanohole channel due to scattering into far-field radiation are so strong that SPP wave excitation on the upper surface is low. Here, most of the field energy inside the channel is directly scattered into far-field radiation and only a small fraction of the field energy is reflected from the upper interface; see Fig. 3(d).

We note that the coupling between SPP waves at both interfaces manifests itself as a splitting in the angle-dependent transmission spectra around $k_x=k_y=0$ (normal incidence of the input pulse). The beat frequency T_{osc}^{-1}, i.e., the coupling strength, gives the magnitude of the splitting. Hence, it is this coupling which is responsible for the band gap formation in these periodic nanostructures.[1,2]

D. Energy flow inside the nanohole channel and on the surface

A detailed study of the plasmon interaction on the two metal surfaces for $d=125$ nm is given in Fig. 5. Figure 5 compares the mean photon flux density $\overline{s_{z,norm}}$ [Fig. 5(a)] to the mean electric energy density $\overline{w_{ex,norm}}$ inside the holes [Fig. 5(b)] and to the photon flux density $\overline{S_{x,norm}}$ on the metal surface, taken at $x=0.15a_0$, i.e., 12.5 nm outside the right edge of the hole [Fig. 5(c)]. We note that if $\overline{S_{x,norm}}>0$, the photon flux is directed *away from* the neighboring hole ($x=y=0$), whereas $\overline{S_{x,norm}}<0$ corresponds to a photon flux directed *towards* the hole. Dashed and solid lines correspond to the lower and upper surfaces, respectively.

The following picture of the plasmon dynamics emerges. The incident femtosecond pulse excites SPP waves at the bottom interface that transfer a photon flux $\overline{S_{x,norm}}$ along x directed towards the neighboring hole [Fig. 5(c)]. These SPP waves couple into the nanohole channel, giving rise to an increase in electric energy density $\overline{w_{ex,norm}}$ at the lower end of the channel, $z=0$, in addition to the input-pulse energy which is directly incident on the bottom hole aperture [Fig. 5(b)]. Though the incident pulse is switched off at $t\approx 40$ fs, the photon flux $\overline{S_{x,norm}}$ on the lower surface still continues, even after that time. This is due to the finite lifetime of the surface plasmon excitations, which is much longer than the input pulse duration.

The increase in energy at the bottom of the hole drives a photon flux $\overline{s_{z,norm}}$ directed towards the upper end of the nanohole channel [Fig. 5(a)]. Hence the energy is transferred from the lower end to the upper end of the channel. The

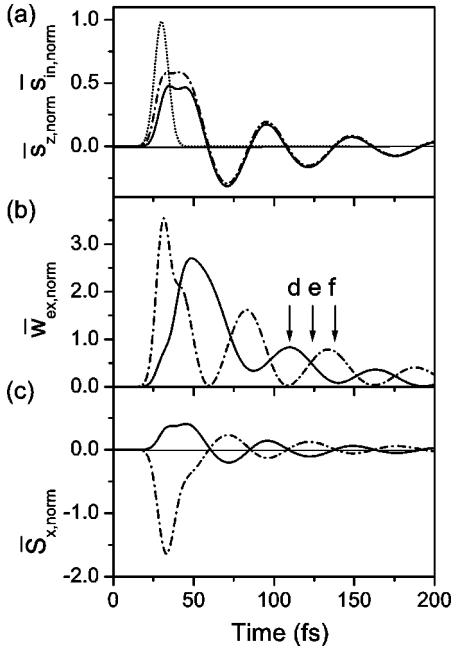

FIG. 5. Time dependence of *photon flux* and *electric field energy* in a metal film with holes of 125 nm diameter (a) Normalized mean *photon flux* density $\overline{s}_{z,norm}$ in a hole at the bottom ($z=0$, dashed curve) and on the top ($z=h$, solid curve) of the metal film; cf. Fig. 3(a). (b) Normalized mean *electric field energy* density $\overline{w}_{ex,norm}$ of the field component E_x in a hole at $z=0$ (dashed curve) and $z=h$ (solid curve). Labels d, e, and f indicate times (110, 125, and 135 fs) at which the *spatial* field distributions are given; see Fig. 6. (c) Normalized *photon flux* density directed along x, $\overline{S}_{x,norm}$, on the bottom surface (dashed curve) and on the top surface (solid curve) at $x=0.15a_0$, $y=0$, on the right side of the hole at $x=0$, $y=0$. The incident signal is a 10-fs pulse shown in (a).

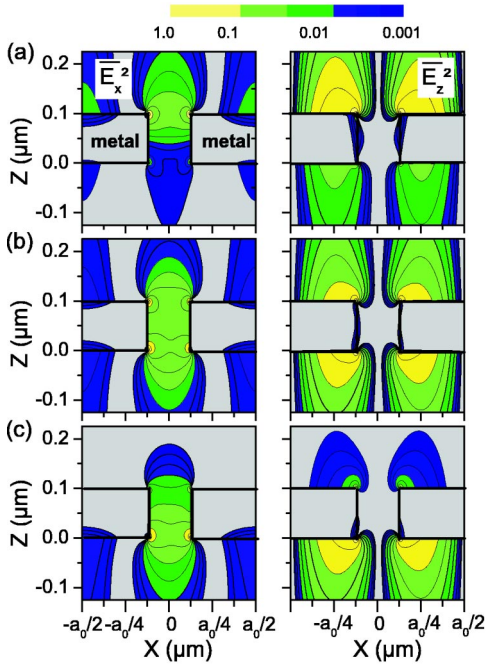

FIG. 6. (Color online) Time-averaged squared field strengths $\overline{E_x^2}$ (left) and $\overline{E_z^2}$ (right) in the x-z plane of a unit cell around a single hole ($d=125$ nm) at three different times: (a) $T=110$ fs, (b) $T=125$ fs, and (c) $T=135$ fs (logarithmic scale for $\overline{E_x^2}$ and $\overline{E_z^2}$). At these times the 10 fs input pulse already vanished but SPP waves still exist at the nanostructure interfaces. The coupling between the top and bottom surface SPP's (via the air-filled channels in the metal film) leads to a regular change of high and low energy densities on the opposite surfaces.

energy density inside the hole at the upper end of the channel then induces a photon flux $\overline{S}_{x,norm}$ on the upper surface along x, directed away from the hole.

The energy density $\overline{w}_{ex,norm}$ inside the hole on the bottom surface approaches zero at $t\approx 60$ fs [Fig. 5(b)] and, simultaneously, both the photon fluxes $\overline{s}_{z,norm}$ and $\overline{S}_{x,norm}$ disappear [Figs. 5(a) and 5(c)]. On the other hand, the energy level of $\overline{w}_{ex,norm}$ on the upper interface is high at that time [Fig. 5(b)]. Therefore, $\overline{w}_{ex,norm}$ is able to drive a photon flux $\overline{s}_{z,norm}$ down the nanohole channel, $t>60$ fs, which transfers energy from the top to the bottom surface—just the reverse situation as that described before. Thus, a periodic oscillation of the energy between lower and upper interfaces is induced. As discussed above, this oscillation is damped by scattering and absorption losses.

E. Spatial distribution of the electric energy density

So far, we have studied the dynamics of light propagation at fixed spatial positions. Now, we analyze the *spatial* structure of the field distributions and their changes in time. We show that these results give a consistent physical picture of light propagation through periodic nanohole arrays.

Figure 6 shows the time-averaged squared electric field strengths $\overline{E_x^2}$ (left) and $\overline{E_z^2}$ (right) in the x-z plane ($y=0$) at times (a) $T=110$ fs, (b) $T=125$ fs, and (c) $T=135$ fs. The spatial distribution of the different quantities is plotted on a logarithmic scale. We note that the numerical simulations show slight deviations from the theoretically expected symmetry with respect to the hole axis ($x=0$). This minor asymmetry is due to the small errors that arise when discretizing the cylindrical apertures on a rectangular grid.

We find high levels of $\overline{E_x^2}$ and $\overline{E_z^2}$ at the top and bottom metal surfaces, not only inside, but also outside the holes, in particular for $\overline{E_z^2}$. In accordance with Fig. 5(b), the intensities at $T=110$ fs [Fig. 6(a); Fig. 5(b), label d] are localized at the top interface. In contrast, at $T=125$ fs [Fig. 6(b); Fig. 5(b), label e] the values at both interfaces are almost identical and at $T=135$ fs [Fig. 6(c); Fig. 5(b), label f] they are localized at the bottom interface.

As can be seen from Fig. 6, both $\overline{E_x^2}$ and $\overline{E_z^2}$ are sharply peaked at the rim of the apertures on the top or bottom surface. This corresponds to the divergencies known from the analytic Bethe-Bouwkamp model for an optical field diffracted by a small aperture in a very thin plane of a perfectly conducting metal.[33,34]

Inside the nanohole channel, the incident SPP field is damped and the field intensity decays along the z axis. A fairly large value of $\overline{E_z^2}$ appears inside the metal along the channel, whereas here $\overline{E_x^2}$ is negligible. This is due to the fact

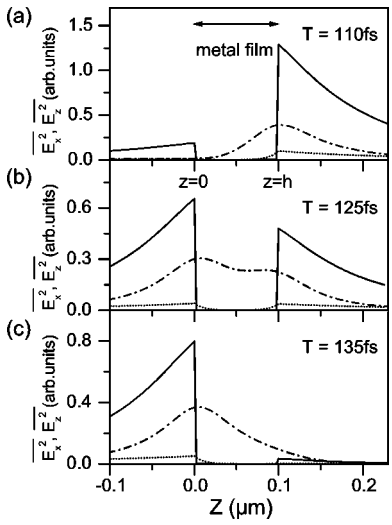

FIG. 7. Time-averaged squared field strengths $\overline{E_x^2}$ and $\overline{E_z^2}$ vs coordinate z at times (a) $T=110$ fs, (b) $T=125$ fs, and (c) $T=135$ fs. The curves show cross sections of $\overline{E_x^2}$ and $\overline{E_z^2}$ along lines parallel to the z axes of Figs. 6(a)–6(c). Solid curves: $\overline{E_z^2}(x=a_0/4)$. Dashed curves: $\overline{E_x^2}(x=0)$. Dotted curves: $\overline{E_x^2}(x=a_0/2)$.

that E_z is parallel to the interface inside the nanohole channel whereas it is perpendicular to the interface on the upper and lower surfaces. The inverse holds for E_x. The SPP field is essentially longitudinal in the metal but transversal in air. Therefore the transverse component of E decays abruptly at the interface, whereas the longitudinal part is exponentially damped inside the metal on a length scale that is given by the skin depth.

Figure 7 displays some of the important features of Fig. 6 in more detail: The solid curves show cross sections of $\overline{E_z^2}$ at $x=\pm a_0/4$ along the z axis, i.e., perpendicular to the plane of the array. The dashed and dotted curves show cross sections of $\overline{E_x^2}$ along z crossing the x axis at $x=0$ or $x=\pm a_0/2$, respectively. The dotted and solid cross sections are taken at the peak values of the $\overline{E_x^2}$ and $\overline{E_z^2}$ standing waves on the metal surfaces at $z=0$, h.

The dotted curves indicate the rapid damping of $\overline{E_x^2}$ at $x=\pm a_0/2$ inside the metal within the skin depth. For $\overline{E_z^2}$, however, a steplike discontinuity occurs at the interfaces. Figure 7 shows that the electric field in air, close to the air/metal interface, has a strong transverse E_z component compared with the longitudinal E_x component. The ratio $\overline{E_z^2}(x=a_0/4,z=h)/\overline{E_x^2}(x=a_0/2,z=h)\approx 13.0$, Fig. 7(a), agrees fairly well with the corresponding ratio $\overline{E_z^2}/\overline{E_x^2}\approx|\varepsilon_1'|\approx 12.5$ for a *planar* surface.[8]

In air, normal to the interfaces, the $\overline{E_x^2}$ curves on the metal film (dotted line) and the $\overline{E_z^2}$ curves (solid line) display an exponential decay, reflecting the strong damping of the SPP field with a decay length of about 150 nm. An analytic expression for the decay constant of $\overline{E_x^2}$ and $\overline{E_z^2}$ is known only for a *planar* interface and reads as $2|k_{sp,z}''|$, with $k_{sp,z}''$ following from $(k_{sp,z}'')^2\cong(\omega/c)^2-k_{sp,x}'^2<0$ (Ref. 8). The decay length $\hat{z}$ of $\overline{E_x^2}$ and $\overline{E_z^2}$ then becomes $\hat{z}=1/(2|k_{sp,z}''|)\approx 130$ nm. This value of $\hat{z}$ agrees quite well with the values taken from the simulation in Fig. 7.

We also find an approximately exponential decay for the field distribution $\overline{E_x^2}$ *inside* the nanohole channel (dashed line in Fig. 7, $0<z<0.1\mu$m). Here, the field intensity decays quite rapidly, on a length scale of about 50 nm.

All together, these results give a quite consistent physical picture of the light transmission through nanohole arrays in metal films. The incident light is scattered at the nanohole grating, transferring momentum $\pm m2\pi/a_0$ to the incident beam and exciting SPP waves at the metal/air interface. To a good approximation, the field distributions of $\overline{E_x^2}$ and $\overline{E_z^2}$ at the metal/air interface can be explained in terms of standing SPP waves, which are generated by interfering counterpropagating E_x or E_z surface fields of wave vector $k_{sp,x}'=\pm 2\pi/a_0$. Contributions from SPP with larger wave vectors $k_{sp,x}'=\pm m2\pi/a_0$, $m\geqslant 2$, are only weakly excited and are less important for achieving high transmission. Within a unit cell around a hole $-a_0/2<x\leqslant a_0/2$, minima of the standing $\overline{E_x^2}$ wave pattern are seen at $x=\pm a_0/4$ in Fig. 6, whereas minima of $\overline{E_z^2}$ waves are found at $x=0$ and $x=\pm a_0/2$. This means that the $\overline{E_x^2}$ and $\overline{E_z^2}$ wave pattern are shifted by $a_0/4$ against each other along the x axis. The calculated spatial distribution for $\overline{E_x^2}$ closely resembles that probed in recent near-field measurements.[16] The sum $\overline{E_x^2}+\overline{E_z^2}$ that is basically the total field energy density is similar to that recently simulated in time-independent calculations for the field amplitude.[14]

This SPP field at the metal/air interface now couples into the nanohole channel. Under our conditions, the nanohole channel can effectively be considered as a cylindrical waveguide beyond cutoff, i.e., $\lambda>\lambda_c$. Its maximum cutoff wavelength $\lambda_c\approx\pi d/1.841$ (Ref. 35) is about 210 nm for $d=125$ nm, and thus much smaller than the incident wavelength of $\lambda=530$ nm. Thus, for a nanohole channel in a perfectly conducting metal, there exists no propagating mode. Only evanescent fields with a purely imaginary propagation constant κ are found inside the channel and coupling through such a channel arises from photon tunneling. As a consequence, the field should decay exponentially along the channel axis with a decay length $L_z=1/|\mathrm{Im}(\kappa)|=1/\sqrt{(2\pi/\lambda_c)^2-(2\pi/\lambda)^2}\approx 38$ nm.

For a real metal with a finite conductivity, a set of modes exists inside the channel which have complex propagation constants with a finite real part. Their imaginary part is reduced giving rise to a decay length that can be substantially, i.e., more than an order of magnitude, larger than L_z for a perfect metal.[21] Due to the finite real part of κ, the time-averaged Poynting vector is generally nonzero and thus a finite power flow exists along the channel, as can be seen in Figs. 3 and 5(a). Our simulations show a decay of the field intensity on a 50 nm scale, i.e., a decay length $L_z=100$ nm, about 3 times larger than for the perfect metal. This indicates that the finite conductivity of the metal enhances the coupling efficiency, which is in qualitative agreement with the result recently obtained in Refs. 21 and 23.

IV. SUMMARY

In summary, we have presented the first fully three-dimensional simulation of ultrafast light propagation through metal films perforated with a periodic array of nanoholes. Studying the propagation of 10-fs pulses shorter than the damping time of SPP excitations, we find pronounced temporal oscillations in the energy flow between the bottom and top interfaces of the metal nanohole grating. These oscillations reflect the coupling of SPP waves at both interfaces through the nanohole channel. The diameter of the nanohole is the main parameter governing the period and damping of these oscillations. For small hole diameters $d<\lambda/2$, the oscillation frequency scales with the cross section of the hole. The damping of the oscillations is given by both the absorption in the metal and the scattering of SPP waves into far-field radiation. The radiation damping scales approximately with the fourth power of the hole diameter, d^4, as for Rayleigh scattering of two-dimensional surface waves.

Our results indicate the following physical picture for the propagation of light through these nanostructures. The incident pulse excites SPP waves at the bottom interface. These couple into the nanohole channel, inducing a transmission of energy through the channel. Part of this energy is stored in SPP excitations at the upper interface. This now induces a photon flux in the opposite direction and eventually a periodic oscillation of the energy between lower and upper interfaces. This oscillation is damped by Ohmic losses in the metal and scattering of the SPP field into far-field radiation. The excitation of SPP waves is directly evidenced by calculating the spatial electric field components E_x and E_z.

The field distribution on the metal surfaces calculated for the longitudinal component (E_x) agrees well with those measured in recent near-field experiments.[16] Similar experiments also support our conclusion that the scattering losses for small hole diameters can be attributed to the Rayleigh scattering of SPP waves at the nanoholes.[6] So far, experimental studies of ultrafast pulse propagation through such nanohole arrays have reported a finite time delay in the transmission. In these experiments, a periodic oscillation of the transmitted light has not been observed. We note that these experiments have been performed on samples with relatively large hole diameters ($d>200$ nm) and with pulses of a duration that is longer than the damping time. Our results indicate that new experiments with shorter pulses shall reveal new insight into the physics of light transmission through nanohole gratings.

ACKNOWLEDGMENT

We thank A. Knorr, J. Förstner, and D. S. Kim for helpful discussions. Financial support by the Deutsche Forschungsgemeinschaft (SFB 296) and the European Union (SQID) is gratefully acknowledged.

[1] T. W. Ebbesen, H. J. Lezec, H. F. Ghaemi, T. Thio, and P. A. Wolff, Nature (London) **391**, 667 (1998).
[2] H. F. Ghaemi, T. Thio, D. E. Grupp, T. W. Ebbesen, and H. J. Lezec, Phys. Rev. B **58**, 6779 (1998).
[3] S. C. Kitson, W. L. Barnes, and J. R. Sambles, Phys. Rev. Lett. **77**, 2670 (1996).
[4] W. L. Barnes, T. W. Preist, S. C. Kitson, and J. R. Sambles, Phys. Rev. B **54**, 6227 (1996).
[5] U. Schröter and D. Heitmann, Phys. Rev. B **60**, 4992 (1999).
[6] D. S. Kim, S. C. Hohng, V. Malyarchuk, Y. C. Yoon, Y. H. Ahn, K. J. Yee, J. W. Park, J. Kim, Q. H. Park, and Ch. Lienau, Phys. Rev. Lett. **91**, 143901 (2003).
[7] *Surface Polaritons*, edited by V. M. Agranovich and D. L. Mills (North-Holland, New York, 1982).
[8] H. Raether, *Surface Plasmons*, Springer Tracts in Modern Physics, Vol. 111 (Springer, Berlin, 1988).
[9] *Near-Field Optics and Surface Plasmon Polaritons*, edited by S. Kawata, Topics in Applied Physics, Vol. 81 (Springer, Berlin, 2001).
[10] I. Pockrand, Opt. Commun. **13**, 311 (1975).
[11] W.-C. Tan, T. W. Preist, and R. J. Sambles, Phys. Rev. B **62**, 11 134 (2000).
[12] R. C. McPhedran, G. H. Derrick, and L. C. Botten, *Theory of Crossed Gratings*, in Topics in Current Physics, Vol. 22, edited by R. Petit (Springer, Berlin, 1980), p. 227.
[13] L. Martin-Moreno, F. J. Garcia-Vidal, H. J. Lezec, K. M. Pellerin, T. Thio, J. B. Pendry, and T. W. Ebbesen, Phys. Rev. Lett. **86**, 1114 (2001).
[14] A. Krishnan, T. Thio, T. J. Kim, H. J. Lezec, T. W. Ebbesen, P. A. Wolff, J. Pendry, L. Martin-Moreno, and F. J. Garcia-Vidal, Opt. Commun. **200**, 1 (2001).
[15] A. Dogariu, T. Thio, L. J. Wang, T. W. Ebbesen, and H. J. Lezec, Opt. Lett. **26**, 450 (2001).
[16] S. C. Hohng, Y. C. Yoon, D. S. Kim, V. Malyarchuk, R. Müller, Ch. Lienau, J. W. Park, K. H. Yoo, J. Kim, H. Y. Ryu, and Q. H. Park, Appl. Phys. Lett. **81**, 3239 (2002).
[17] C. Sönnichsen, A. C. Duch, G. Steininger, M. Koch, G. von Plessen, and J. Feldmann, Appl. Phys. Lett. **76**, 140 (2000).
[18] U. Schröter and D. Heitmann, Phys. Rev. B **58**, 15419 (1998).
[19] M. M. J. Treacy, Appl. Phys. Lett. **75**, 606 (1999).
[20] J. A. Porto, F. J. Garcia-Vidal, and J. B. Pendry, Phys. Rev. Lett. **83**, 2845 (1999).
[21] E. Popov, M. Neviere, S. Enoch, and R. Reinisch, Phys. Rev. B **62**, 16 100 (2000).
[22] L. Salomon, F. Grillot, A. V. Zayats, and F. de Fornel, Phys. Rev. Lett. **86**, 1110 (2001).
[23] S. Enoch, E. Popov, M. Neviere, and R. Reinisch, J. Opt. A, Pure Appl. Opt. **4**, S83 (2002).
[24] S. A. Darmanyan and A. V. Zayats, Phys. Rev. B **67**, 035424 (2003).
[25] I. I. Smolyaninov, A. V. Zayats, A. Stanishevsky, and C. C. Davis, Phys. Rev. B **66**, 205414 (2002).
[26] St. A. Cummer, IEEE Trans. Antennas Propag. **45**, 392 (1997).
[27] *Handbook of Optical Constants of Solids*, edited by E. D. Palik (Academic, Orlando, FL, 1985).
[28] A. Taflove and S. C. Hagness, *Computational Electrodynamics:*

The Finite-Difference Time-Domain Method, 2nd ed. (Artech House, Boston, 2000).

[29] *Advances in Computational Electrodynamics: The Finite-Difference Time-Domain Method*, edited by A. Taflove (Artech House, Boston, 1998).

[30] J. W. Goodman, *Introduction to Fourier Optics* (McGraw-Hill, Boston, 1996).

[31] B. Lamprecht, J. R. Krenn, G. Schider, H. Ditlbacher, M. Salerno, N. Felidj, A. Leitner, F. R. Aussenegg, and J. C. Weeber, Appl. Phys. Lett. **79**, 51 (2001).

[32] A. V. Shchegrov, I. V. Novikov, and A. A. Maradudin, Phys. Rev. Lett. **78**, 4269 (1997).

[33] R. D. Grober, T. Rutherford, and T. D. Harris, Appl. Opt. **35**, 3488 (1996).

[34] A. Chavez-Prison and S. T. Chu, J. Microsc. **194**, 421 (1999).

[35] R. E. Collin, *Field Theory of Guided Waves*, 2nd ed. (Oxford University Press, Oxford, 1990).